Available online at www.sciencedirect.com
ScienceDirect
International Journal of Heat and Fluid Flow 28 (2007) 561–574
International Journal of HEAT AND FLUID FLOW
www.elsevier.com/locate/ijhff

Large eddy simulation of turbulent flow for wall mounted cantilever cylinders of aspect ratio 6 and 10

Imran Afgan [a,*], Charles Moulinec [a,b], Robert Prosser [a], Dominique Laurence [a,b]

[a] University of Manchester, George Begg. Building, MACE, P.O. Box 88, Manchester M601QD, UK
[b] Electricité de France R&D, 6 quai Watier, 78400 Chatou, France

Received 22 November 2006; received in revised form 30 March 2007; accepted 18 April 2007
Available online 6 June 2007

Abstract

The flow structure around wall mounted circular cylinders of finite heights is numerically investigated via large eddy simulation (LES). The cylinder aspect ratios (AR) are 6 and 10 and the Reynolds number *(Re)* based on cylinder diameter and free stream velocity is 20,000 for both cases. The cantilever cylinder mounted on a flat plate is chosen since it gives insight into two entirely different flow phenomena; the tip effects of the free end (which show strong three-dimensional wake structures) and the base or junction effects (due to interaction of flow between the cylinder and the flat plate). Regular vortex shedding is found in the wake of the higher aspect ratio case as was anticipated, along with a strong downwash originating from the flow over the free end of the cylinder, whereas irregular and intermittent vortex shedding occurs in the lower aspect ratio case. Pressure distributions are computed along the length of the cylinder and compared to experimental results. Lift and drag values are also computed, along with Strouhal numbers.

Keywords: Embedded refinement; Finite cylinder; Free end effect; Large eddy simulation; Unstructured finite volumes; Vortex shedding

1. Introduction

A cantilever cylinder with one end fixed and the other free to vibrate has been numerically simulated to study the dynamics of turbulent flow around cylinder bodies. The long-term objective of this study is to apply large eddy simulation (LES) to flow induced vibrations (FIV). The present fixed cylinder case is intended to serve as a validation and to provide an analysis insight into the flow-physics. These cases are a continuation of the work of Frohlich and Rodi (2004), in which the authors tested a cylinder with an aspect ratio (AR) of 2.5 and recommend testing of further AR cases at the same subcritical Reynolds number (*Re*) range ($2 \times 10^4 < Re < 2 \times 10^5$).

It has been observed that the flow over a finite cylinder's free end has a complicated three-dimensional wake structure; the free end plays a direct and significant role in providing 3D flow characteristics over all Reynolds number ranges (Park and Lee, 2000). The wake structure is due to the counter rotating vortices generated by the free end itself. In cylinders with both ends fixed however the scenario is somewhat different where the fluid must first be accelerated and then displaced sideways in order to pass over the cylinder body and enter the wake region.

The applications of finite cylinders are numerous, including tall rising buildings in city centres and nuclear cooling towers. At lower Reynolds numbers, one finds applications in internal components of nuclear plants such as fuel or control rods and various instrumentations. Notable papers containing extensive experimental data on such configurations are those of Park and Lee (2000, 2002, 2004) and that of Okajima et al. (2002). In the current study, the flow over two such configurations with aspect ratio of 6 and 10 is numerically simulated and then compared to

* Corresponding author. Tel.: +44 161 306 3710; fax: +44 161 306 3755.
E-mail addresses: I.Afgan@postgrad.manchester.ac.uk, afgan_imran@hotmail.com (I. Afgan), chmoulinec@yahoo.com (C. Moulinec), Robert.Prosser@manchester.ac.uk (R. Prosser), dominique.laurence@manchester.ac.uk (D. Laurence).

0142-727X/$ - see front matter © 2007 Elsevier Inc. All rights reserved.
doi:10.1016/j.ijheatfluidflow.2007.04.014

Nomenclature

A	projected area of the cylinder (m^2)
AR	height to diameter ratio $[H/D]$ (–)
C	cross-sectional area of grid in YZ plane (m^2)
C_D	drag coefficient $\left[\frac{2F_X}{A\rho U_0^2}\right]$ (–)
C_L	lift coefficient $\left[\frac{2F_Y}{A\rho U_0^2}\right]$ (–)
C_P	pressure coefficient $\left[\frac{2(P-P_{ref})}{\rho U_0^2}\right]$ (–)
C_S	Smagorinsky coefficient (–)
D	diameter of cylinder (m)
DES	detached eddy simulation (–)
FIV	flow induced vibrations (–)
F_X	total drag force (N)
F_Y	total lift force (normal to streamwise and height) (N)
f	vortex shedding frequency (1/s)
H	height of the cylinder (m)
H_Z	total height of the computational domain (m)
L_C	characteristic length scale (m)
LES	large eddy simulation (–)
LES-NWR	large eddy simulation-near wall resolution (–)
P	pressure (N/m^2)
P_{ref}	reference pressure (N/m^2)
Q	second invariant of velocity magnitude $\left[-\frac{1}{2}\left(S_{ij}S_{ij}-\Omega_{ij}\Omega_{ij}\right)\right]$ (–)
Re	Reynolds number $\left[\frac{\rho U_0 D}{\mu}\right]$ (–)
SGS	subgrid-scale (–)
$\|\|S\|\|$	filtered strain rate magnitude $\left[\sqrt{2S_{ij}S_{ij}}\right]$ (1/s)
S_{ij}	strain rate tensor $\left[\frac{1}{2}\left(\frac{du_i}{dx_j}+\frac{du_j}{dx_i}\right)\right]$ (1/s)
St	Strouhal number $\left[\frac{fD}{U_0}\right]$ (–)
Tu%	streamwise turbulence intensity percentage $\left[\frac{\sqrt{\langle u'u'\rangle}}{U_0}\times 100\right]$ (–)
U_0	inlet velocity (m/s)
u_i, u_j	velocity tensor (m/s)
u^*	wall friction velocity $\left[\left(\frac{\tau_w}{\rho}\right)^{1/2}\right]$ (m/s)
Vol	cell volume (m^3)
Y^+	non-dimensional cell distance from wall $\left[\frac{u^* y}{v}\right]$ (–)
$\bar{\Delta}$	filter length (m)
δ	boundary layer thickness $\left[\delta\sim\left(\frac{vx}{U_0}\right)\right]$ (m)
μ	dynamic viscosity ($kg\,s/m^2$)
v	kinematic viscosity (m^2/s)
v_t	SGS viscosity (m^2/s)
Ω_{ij}	rotational rate tensor $\left[\frac{1}{2}\left(\frac{d\overline{u_i}}{dx_j}-\frac{d\overline{u_j}}{dx_i}\right)\right]$ (1/s)
ω_z	vorticity in z direction $\left[\left(\frac{d\overline{u_1}}{dx_2}-\frac{d\overline{u_2}}{dx_1}\right)\right]$ (1/s)
ρ	density of fluid (kg/m^3)
τ_w	wall shear stress (N/m^2)
τ_{ij}	stress tensor (N/m^2)
x_i, x_j	distance tensor (m)

Subscripts and superscripts

$'$	fluctuating component
$-$	filtered quantity
$\langle\rangle$	time averaged quantity

experimental results. A non-conforming local mesh refinement is implemented in all three spatial directions to reduce the size of the computational grid required to resolve the finite cylinder which poses a huge computational grid requirement.

2. Flow geometry

The geometry consists of a finite circular cylinder vertically mounted on a flat plate with one end fixed and the other free (and in later cases also allowed to vibrate, not considered here). The vortices that are shed from the cylinder, along with a strong downwash from its free end require a fairly long computational domain to capture the flow physics adequately. The downstream length is set at 36 diameters and the upstream length is set at 12 diameters, with the origin of the coordinate system located at the centre of the base of the cylinder. The complete geometry is shown in Fig. 1, where a uniform flow enters from the left. The blockage ratio defined as the ratio of the projected cylinder area to the cross-sectional area of test section (A/C) is 1.38% for AR 6 test case and 2.31% for the AR 10 test case, which is well within the prescribed range for cylinder flows (where the maximum blockage ratio allowed for such flows is 3%; Zdravkovich, 1997). However a little variation in this ratio is still acceptable; Frohlich and Rodi (2004) use a blockage ratio of 7.1% for all their simulations, still achieving decent results as

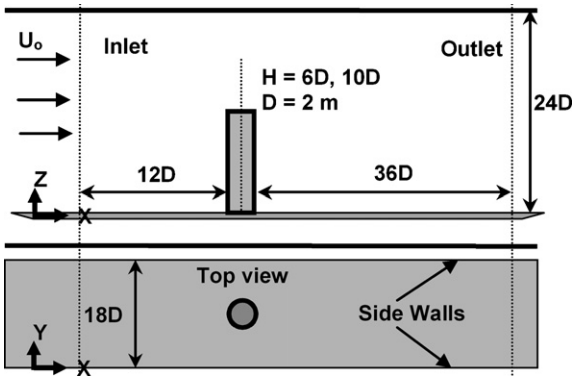

Fig. 1. Geometry under consideration of finite cylinder. Top: Cross-sectional view in XZ plane. Bottom: Cross-sectional view in XY plane.

compared to experiments. While understanding the tip flow effects special consideration should also be given to the height of the computational domain. In the present case this total height (H_Z) is 24 diameters. Thus the ratio $H_Z/H = 4$ for AR 6 case and 2.4 for AR 10 case which is still sufficiently larger than the experimental (Park and Lee (2000)) ratios of 3.33 and 2 for AR 6 and 10 cases, respectively.

3. Numerical treatment

A prototype[1] version of the commercial code *STAR-CD V4* is used to solve 3D Navier–Stokes equations on the unstructured grids using finite volume approach.

The flow is assumed to be Newtonian and incompressible. For LES the filtered Navier–Stokes equations are given by

$$\begin{cases} \frac{\partial \overline{u}_i}{\partial t} + \frac{\partial \overline{u}_i \overline{u}_j}{\partial x_j} = -\frac{1}{\rho}\frac{\partial \overline{p}}{\partial x_i} + \nu \frac{\partial^2 \overline{u}_i}{\partial x_j \partial x_j} - \frac{\partial \tau_{ij}}{\partial x_j}, \\ \frac{\partial \overline{u}_i}{\partial x_i} = 0, \quad i \in \{1,2,3\} \end{cases} \tag{1}$$

For the subgrid-scale modelling (SGS), the standard Smagorinsky model is used;

$$\tau_{ij} - \frac{1}{3}\tau_{kk}\delta_{ij} = -2\nu_t \overline{S}_{ij} = -2(C_S \overline{\Delta})^2 \|S\| \overline{S}_{ij} \tag{2}$$

where $\overline{S}_{ij}$ is the filtered strain rate tensor ($\|S\| = \sqrt{2\overline{S}_{ij}\overline{S}_{ij}}$). As the cells used in the present work are hexahedral we can take the filter width to be twice that of the cube root of the cell volume ($\overline{\Delta} = 2\mathrm{Vol}^{1/3}$). The Smagorinsky constant[2] (C_S) is set to 0.065 and is locally damped by a Van Driest wall damping function near solid walls. In the collocated finite volume approach used here, all variables are located at the centres of the cells (which can be of any shape) and the momentum equations are solved by considering an explicit mass flux and a fully centred convection scheme. Pressure–velocity coupling is ensured by a prediction/correction method using the SIMPLEC algorithm; Van Doormal and Raithby (1984) also described in Ferziger and Peric (2002). The Poisson equation is solved using a conjugate gradient method. This collocated discretization requires Rhie and Chow (1982) interpolation in the correction step to avoid oscillatory solutions.

The three time level implicit time advancing scheme (TTLM) of Ferziger and Peric (2002), is used for time discretization. This scheme performs the time integration over an interval centered at the new time level and is second order accurate. The non-orthogonalities are taken into account with a reconstruction technique explained in Ferziger and Peric (2002) and are tested for LES by Benhamadouche and Laurence (2003), and Bouris and Bergeles (1999). When a non-orthogonal grid is used, the matrix contains the orthogonal contribution only and the non-orthogonal part is solved explicitly; this is known as the deferred correction. However, one can iterate on the system to make it quasi-implicit.

The suitability of this commercial code for LES taking into consideration the global value of Smagorinsky constant (C_S) and effects of various discretization schemes has been extensively tested at University of Manchester on homogeneous grid turbulence, channel flows and in-line cylinders; Laurence (2006), Moulinec et al. (2005) and Benhamadouche et al. (2005). In Moulinec et al. (2005) the conservation of kinetic energy using collocated unstructured finite volumes was discussed, and a recommended action was to use polyhedral or Cartesian cells with localized refinement rather than a tetrahedral mesh. Conserving kinetic energy not only eliminates numerical diffusion, but also ensures a bounded solution even with pure central differencing schemes, such as those used here. Upwinding, even in small quantity or via higher order terms is not suitable for LES; see Grotzbach and Worner (1999) and Kravchenko and Moin (1997).

4. Grid independence study

A grid independence study was conducted prior to launching the final simulations. For the larger AR case, three meshes were tested, coarse non-conforming mesh (CNCM1), fine non-conforming mesh (FNCM1) and a fine conforming mesh (CM). For the smaller AR case, two non-conforming meshes were tested; coarse non-conforming mesh (CNCM2) and fine non-conforming mesh (FNCM2). A list of the five meshes used is given in Table 1.

The grid generation process was manually controlled to ensure that the overall computational resource requirement was minimized. Thus, the biggest constraint was to limit the grid to be less than 4 million cells in-line with available computational resources (8–12 CPUs of an in-house Beowulf cluster). The numerical results from private communications (contributions of Strelets (2005) and Krajnovic (2006) to the DESider database; see acknowledgements) were used for quantitative comparisons in some cases but are not reported in this paper. The first Strelets (2005) results are based on a grid of 2 million cells for detached eddy simulation (DES). However the present LES grids (FNCM1, CM and FNCM2) in comparison are

[1] Simulations started early 2005 using a pre-release made available by CD-adapco, whereas *STAR-CD V4* became commercially available in spring 2006. Recent channel and pipe flow LES test cases at Manchester with both versions demonstrated the same results and numerical performance.

[2] Note the factor 2 in the filter width, i.e. for a cubical cell the filter width is twice the mesh step, as in Moin and Kim (1982) and Pope (2000).

Table 1
Overview of the grid independence study: cases simulated, meshes tested for each case and the total number of cells in each mesh

	Case 1: AR 10			Case 2: AR 6	
Mesh	CNCM1	FNCM1	CM	CNCM2	FNCM2
Total grid cells	1.1×10^6	2.6×10^6	3.4×10^6	0.9×10^6	1.8×10^6

of the same fineness level near the cylinder surface and flat plate, significantly finer at the tip of the cylinder, but fairly coarse in the far field. This was achieved by use of non-conforming refinement in all directions. The interface cells are not treated as "embedded grids", but as polyhedral cells with more than six faces, i.e. the cell-face based algorithm is the same whatever the number of faces and no special treatment is introduced between regions of different refinement. A total of nine levels of local refinement have been used with the cell size change ratio limited to a maximum of 33% in every case (i.e. three cells matching with two cells rather than two facing one as this latter case has been observed to lead to oscillations in some cases, see Laurence, 2006). Thus for every direction the grid has three levels of non-conforming refinements. Fig. 2 shows a number of views of the computational grids (FNCM1 and CM) with local refinement in different directions. Here the large eddy simulation with near wall resolution (LES-NWR) approach is implemented (Pope, 2000), where the filter and grid are both sufficiently fine to resolve 80% of the energy everywhere. The first cells normal to the cylinder surface along the azimuthal axis are fixed at $Y^+ \approx 1$ compared to the $Y^+ \approx 5$ for the flat plate which is reasonable enough to model the near wall damping effect. Admittedly this may not be fine enough for an accurate reproduction of boundary layer development, but the boundary layer thickness is fairly short in the experiments ($\delta \sim 6\%D$), since a uniform inlet profile is implemented at the inlet of the flow domain and the distance between the leading edge of the flat plate and the finite cylinder is around 12–16D for both experiments and CFD computations.

For the numerical simulations, the side and top surfaces are kept as slip walls to reduce the size of the computational mesh. The solid cylinder surface and the flat bottom plate are treated as no-slip walls. At the inlet, a constant boundary condition with $U = U_0$ (no fluctuations) is prescribed, similar to the experiments (Park and Lee, 2000). At the outlet, convective outflow boundary condition is imposed. These boundary conditions are consistent with those already tested for similar test cases (Frohlich et al., 1998; Frohlich and Rodi, 2004). The LES simulations are run for 20 complete flow cycles, with time averaging of results performed over the last 10–12 cycles.

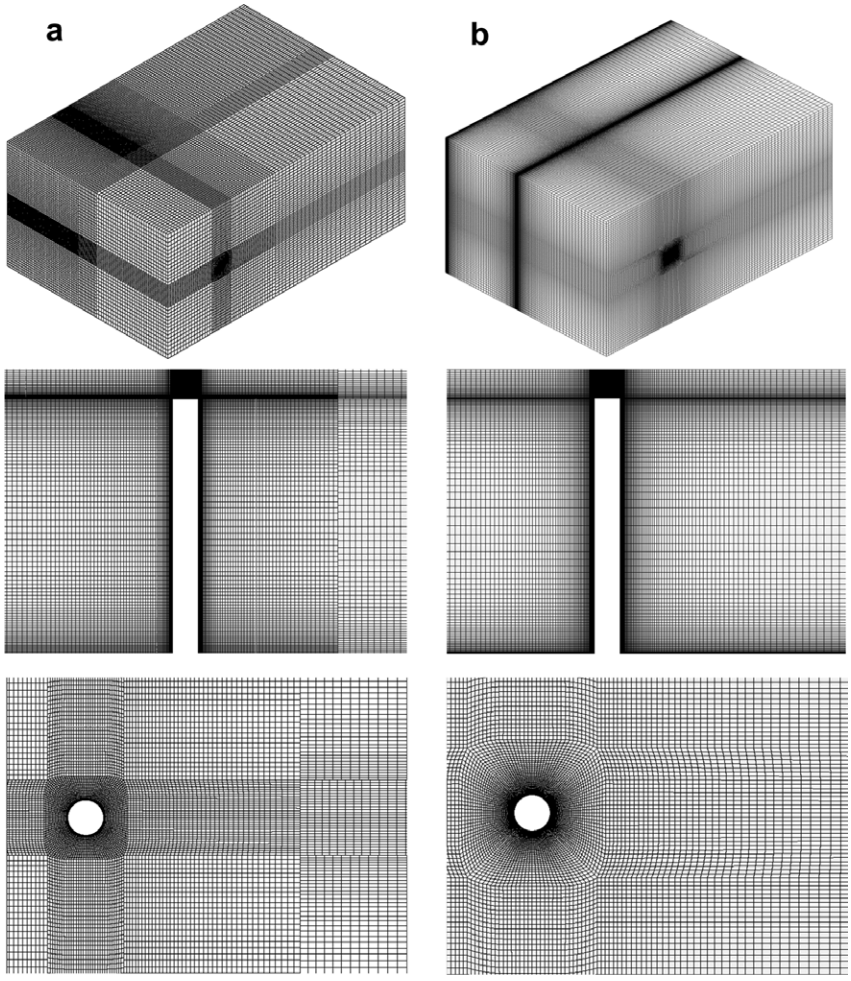

Fig. 2. Various orthogonal and sectional views of the grid for AR 10 case: (a) Non-conforming mesh with local refinement (FNCM1). (b) Regular mesh (CM). 3D view of the complete grid (top), sectional view in XZ plane (middle) and sectional view in XY plane (bottom).

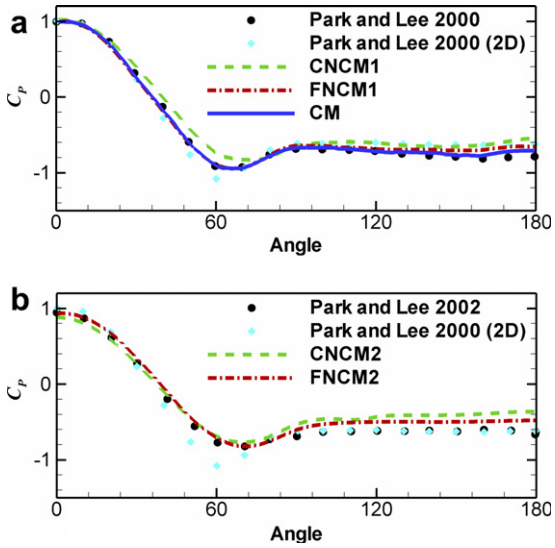

Fig. 3. C_P profile around the cylinder: (a) Case 1 (AR 10) at $Z/L = 0.883$ (Experiment of Park and Lee (2000), CNCM1, FNCM1 and CM). (b) Case 2 (AR 6) at $Z/L = 0.5$ (Experiment Park and Lee (2002), CNCM2 and FNCM2).

Fig. 3 shows a comparison between the pressure coefficients (C_P) obtained from various grids and the experimental data, where (C_P) is defined as $C_P = 2(P - P_{ref})/\rho U_0^2$. However, as the pressure is variable along the vertical stagnation line, the data has been rescaled with a variable reference pressure $P_{ref}(Z)$ such that $C_{PMax} \approx 1.0$ for each altitude (to maintain consistency with the experimental results). Fig. 3a shows the comparison between results from CNCM1, FNCM1 and CM for the higher aspect ratio case (AR 10) at $Z/L = 0.883$. Fig. 3b shows a comparison between results from CNCM2 and FNCM2 for the lower aspect ratio case (AR 6) at $Z/L = 0.50$. For comparison both these figures show the experimental C_P profile for an infinite cylinder at the same *Re* number of 20,000. From Fig. 3a one sees almost no change in the predicted C_P profile with the use of CM over FNCM1, demonstrating that the non-conforming cells introduce no adverse effects. With the coarse grid, CNCM1, the negative peak is not fully captured, with a general trend of slightly over predicting pressure in most of the wake-side. In Fig. 3b for the lower aspect ratio, the coarser CNCM2 shows the same slight over prediction of wake-side pressure levels as compared to FNCM2 and experiments. The fully conforming mesh is not tested for case 2 since no marked improvement was seen in case 1 with such a mesh, admitingly FNCM2 still slightly under predicts the pressure profile and results in a slightly bigger recirculation region in the wake of the cylinder in both *XY* and *XZ* plane. This has been a common observation in all numerical simulations; FNCM1, FNCM2, CM, DES (Strelets, 2005) and very fine LES (Krajnovic, 2006). Thus the finer grids FNCM1 and FNCM2 are chosen for AR 10 and AR 6 test cases, respectively, and their results are reported in detail in the following section.

5. Discussion of results

5.1. Pressure distribution

Fig. 4 shows the vertical mean pressure on the finite cylinder along the stagnation line (0°) and wake line (180°), normalized by the dynamic pressure based on inlet uniform velocity and the reference pressure behind the cylinder at the flat plate junction (180° and $Z/D = 0$). The pressure profile at the front is almost constant then drops sharply at $-1/4D$ from the tip. In Fig. 4a at the back side (180°) near the tip of the cylinder a sharp depression is seen in the pressure profile which corresponds to the vortex core shown in Fig. 7. It is seen that at $-1/4D$ from the tip ($Z - H = -0.25D$) a sharp recovery is produced by the backflow below the tip vortex. Then, between $-1/4D$ and $-3D$ from the tip, a more gradual recovery is observed, resulting from a 3D backflow which is observed from both cross-stream and vertical symmetry plane plots in Figs. 6 and 7.

Fig. 5a and b shows the mean C_P profiles around the cylinder surface for AR 10 (FNCM1) and AR 6 (FNCM2) cases, respectively, for a number of vertical (Z/L) locations. These C_P profiles are in fairly close agreement with the experimental values of Park and Lee (2000, 2002) up to the minimum located at 70–80°. The pressure recovery is slightly slower in the simulations, but the pressure plateau is again well predicted. Beyond 160° the pressure is very much influenced by tip effects.

Fig. 5a shows the plots for AR 10 case at $Z/L = 0.983$, $Z/L = 0.95$, $Z/L = 0.933$, $Z/L = 0.9$ and $Z/L = 0.883$ (from top to bottom, respectively). The pressure recovery behind the cylinder near the tip is more pronounced, where both experimental and numerical results show this sharp pressure rise in the wake of the cylinder (top left plot in Fig. 5a). The pressure recovery is still visible for $Z/L = 0.9$ which corresponds to $-1D$ from the tip. However, the downwash effect (which is very strong in the smaller aspect ratio case) is now somewhat reduced, leading to regular vortex shedding in the lower half of the cylinder. For the AR 6 case (Fig. 5b) the profiles are plotted at $Z/L = 0.983$, $Z/L = 0.944$, $Z/L = 0.917$, $Z/L = 0.806$ and $Z/L = 0.5$ (from top to bottom). For this case a fairly stronger downwash is observed which tends to suppress regular vortex shedding in the lower half of the cylinder. Note that for AR 6 case the third graph from top in Fig. 5b which is at $Z/L = 0.917$ and the second graph from the top for AR 10 case in Fig. 5a which is at $Z/L = 0.95$ both correspond to $-0.5D$ from the tip of the cylinder. Hence the pressure rise due to the tip effect is now much less visible. Experimental findings of Park and Lee (2000, 2002, 2004) only report such a pressure rise for the aspect ratio 10 case. One can thus conclude, somewhat surprisingly, that the flow structure at the very tip of the cylinder is quite different for AR 6 and AR 10 cases.

At $Z/L = 0.5$ the *DES* results of Strelets (2005) reported in Afgan et al. (2006), the present LES and the ongoing

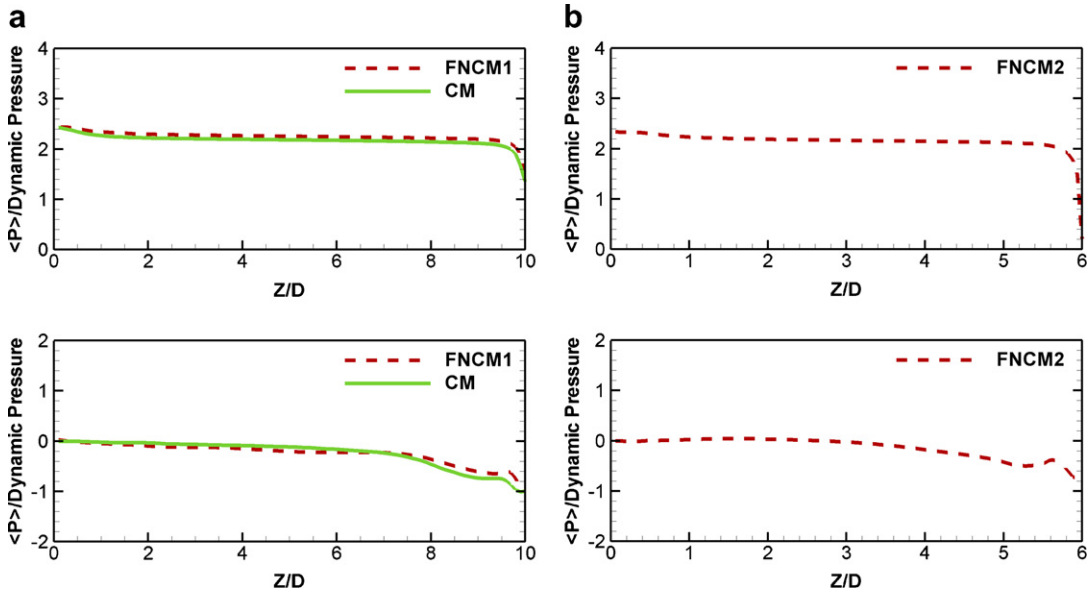

Fig. 4. Pressure profile along cylinder axis, top: along stagnation line at 0°, bottom: along wake line at 180° (a) AR 10 case (b) AR 6 case.

(not shown here) fine LES by (Krajnovic, 2006) tend to show a somewhat higher plateau than the experimental profile in the leeward side of the cylinder. In any case the plateau for all data is significantly higher than that found in the case of an infinite cylinder at similar Reynolds number. This pressure recovery is accompanied by the suppression of vortex shedding behind the cylinder. Experimental findings of Park and Lee (2000) report irregular and weak vortex shedding for the AR 6 case; numerical simulations on the other hand predict intermittent yet barely visible vortex shedding as if the downwash effect is almost strong enough to totally suppress the vortex shedding.

For cantilever cylinders, as the aspect ratio decreases the vortex shedding frequency also decreases, but the classification of vortex shedding behind the cylinder depending on the aspect ratio is a debatable issue. Various experimental and numerical results have failed to reach a consensus on the vortex shedding character. According to Farivar (1981), the regular vortex shedding disappears for cylinders with an aspect ratio lower than 7.5. Zdravkovich et al. (1989) on the other hand found regular vortex shedding behind a cantilevered cylinder with an aspect ratio of 4. Kawamura et al. (1984) discuss in detail the critical length of a finite cylinder after which vortex shedding is totally suppressed. However, the number of influencing parameters are many: Reynolds number, aspect ratio, blockage effects, approaching boundary layer thickness and free stream or inlet turbulence intensity. While an exact definition of the former three parameters is relatively easy, duplicating the latter two parameters can be somewhat problematic, especially the approaching boundary layer thickness (which itself depends on a number of other parameters such as upstream length, Reynolds number etc.). Hence drawing a clear limiting value of aspect ratio where vortex shedding is totally suppressed is not possible at present, although the current flow is classified to fall into the subcritical regime ($2 \times 10^4 < Re < 2 \times 10^5$) by Zdravkovich (1997).

5.2. Velocity distribution

Mean velocity streamlines in XY plane for the smaller aspect ratio case (AR 6) are shown in Fig. 6 at various Z/L locations. It is interesting to note that a pair of narrow recirculation bubbles in the wake generates a strong and wide backflow (towards the cylinder). This is a significantly different pattern from the infinite cylinder C_P plateau shown in Fig. 3b. Fig. 7 shows the streamlines generated from 2D mean velocity vectors in the vertical symmetry plane ($Y/D = 0$). Over the tip of the cylinder the maximum velocity (which at the inlet is 10 m/s) goes as high as 14 m/s. A dense cluster of lines generated just before the tip of the cylinder later highlights the strong arc shaped downstream, almost reaching the base plate. The location of this arc corresponds in Fig. 6 to the saddle point marking the end of the vortex pair. Thus the streamline divergence along the arc in Fig. 7 highlights the strong 3D effects and the curved arc shows that the size of the recirculating vortex pair in Fig. 6 is highly variable with altitude. Hence for the AR 6 cylinder, even at mid-height one should not expect results to match closely to that of an infinite cylinder. Near the tip the recirculation (in XZ plane) is much smaller, similar to the findings of Frohlich and Rodi (2004), Kawamura et al. (1984) and Zdravkovich (1997). At the foot of the cylinder, in front, streamlines are seen to curve back towards the plate, just about suggesting a horseshoe vortex but this one is very shallow, as shown in Fig. 12. Behind the cylinder at the cylinder plate junction

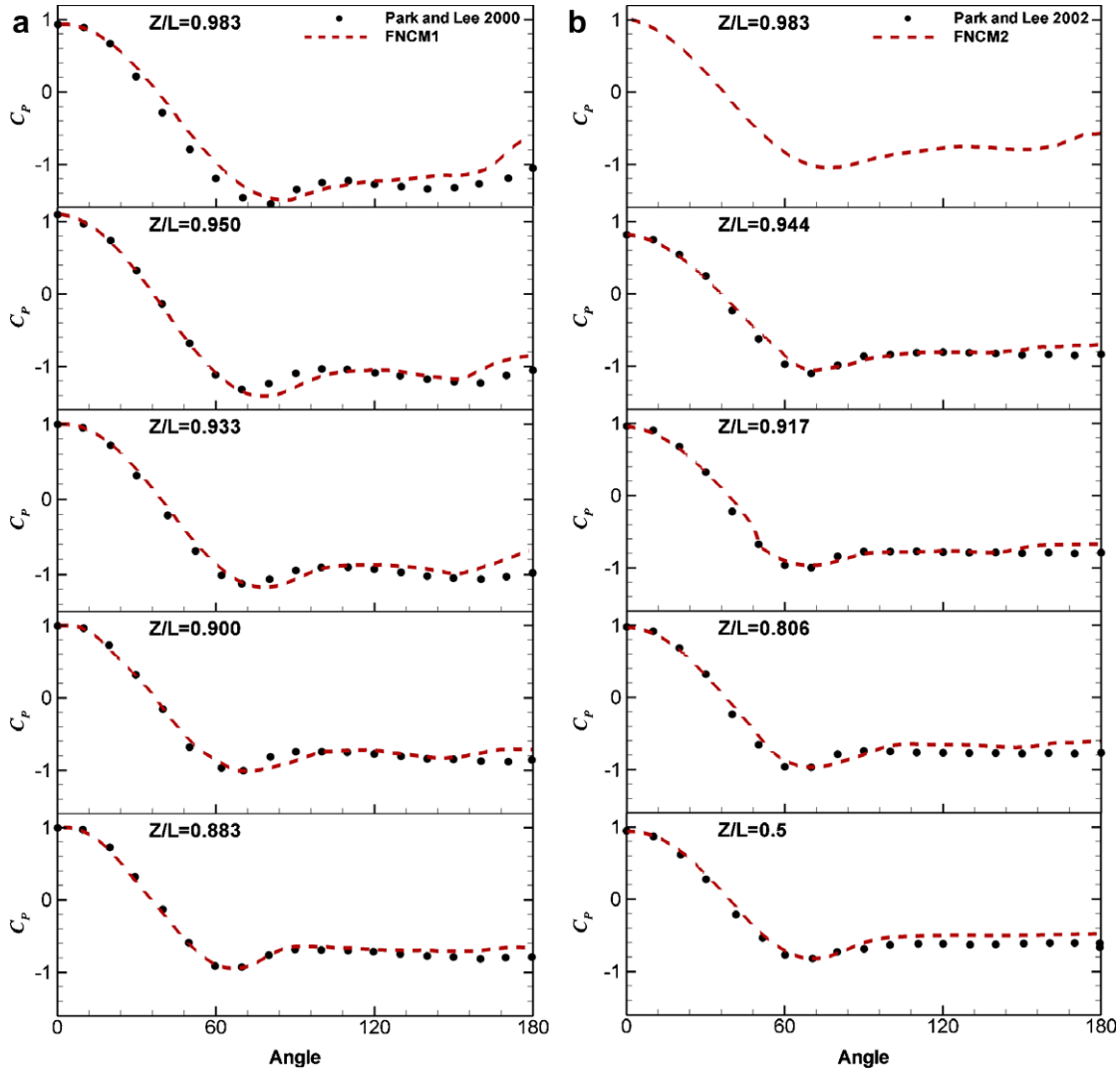

Fig. 5. C_P profile along the cylinder surface: (a) AR 10 case (from top to bottom $Z/L = 0.983$, $Z/L = 0.95$, $Z/L = 0.933$, $Z/L = 0.9$ and $Z/L = 0.883$, respectively). (b) AR 6 case (from top to bottom $Z/L = 0.983$, $Z/L = 0.944$, $Z/L = 0.917$, $Z/L = 0.806$ and $Z/L = 0.5$, respectively).

a second vortex is seen resulting from the downwash all along the cylinder, but this one is fully embedded in the near wake and is unrelated to the horseshoe vortex.

The mean streamwise velocity profile is shown in Fig. 8 in the wake of the cylinder at two different locations ($X/D = 5$ and 10). One observes that the higher aspect ratio case (Fig. 8a) has a narrow wake as compared to the smaller case (Fig. 8b). This is consistent with the fact that with an increasing aspect ratio the flow behaviour becomes that of a 2D cylinder. Naturally, one would also expect that the effect of the downwash reduces in intensity as one moves away from the cylinder tip both in streamwise (downstream) and spanwise directions (along the height of the cylinder). However, this behaviour is quite different for the two cases under consideration. The higher aspect ratio (AR 10) case has a significantly longer recirculation (in XZ plane) bubble and hence the reduction in velocity is not very high near the base of the cylinder at the two monitoring stations ($X/D = 5$ and 10). This can also be observed with the double velocity peak at $Z/H = 0.75$ location in Fig. 8a. For the smaller aspect ratio (AR 6) case this effect of downwash is more focused along the height of the cylinder rather than its wake, hence a shorter recirculation bubble is observed but with a greater reduction in velocity near the cylinder base.

The contour plot of secondary flow $(\bar{v}^2 + \bar{w}^2)^{1/2}$ along with average pseudo-streamlines for the AR 10 case (FNCM1) downstream of the cylinder at various X/D locations is shown in Fig. 9 (this is constructed from the 2D flow-field in that plane and does not correspond to a projection of 3D streamlines). Here, pseudo-average streamlines provide a clearer picture of the inverted U of the arch vortices which were discussed earlier. These vortices generated from the tip of the cylinder travel downstream and downwards at the same time vanishing at around 5D downstream of the cylinder (Fig. 9d). It is also observed from the same figure that the effect of these tip vortices travels until a maximum of 2.4D height of the cylinder (also

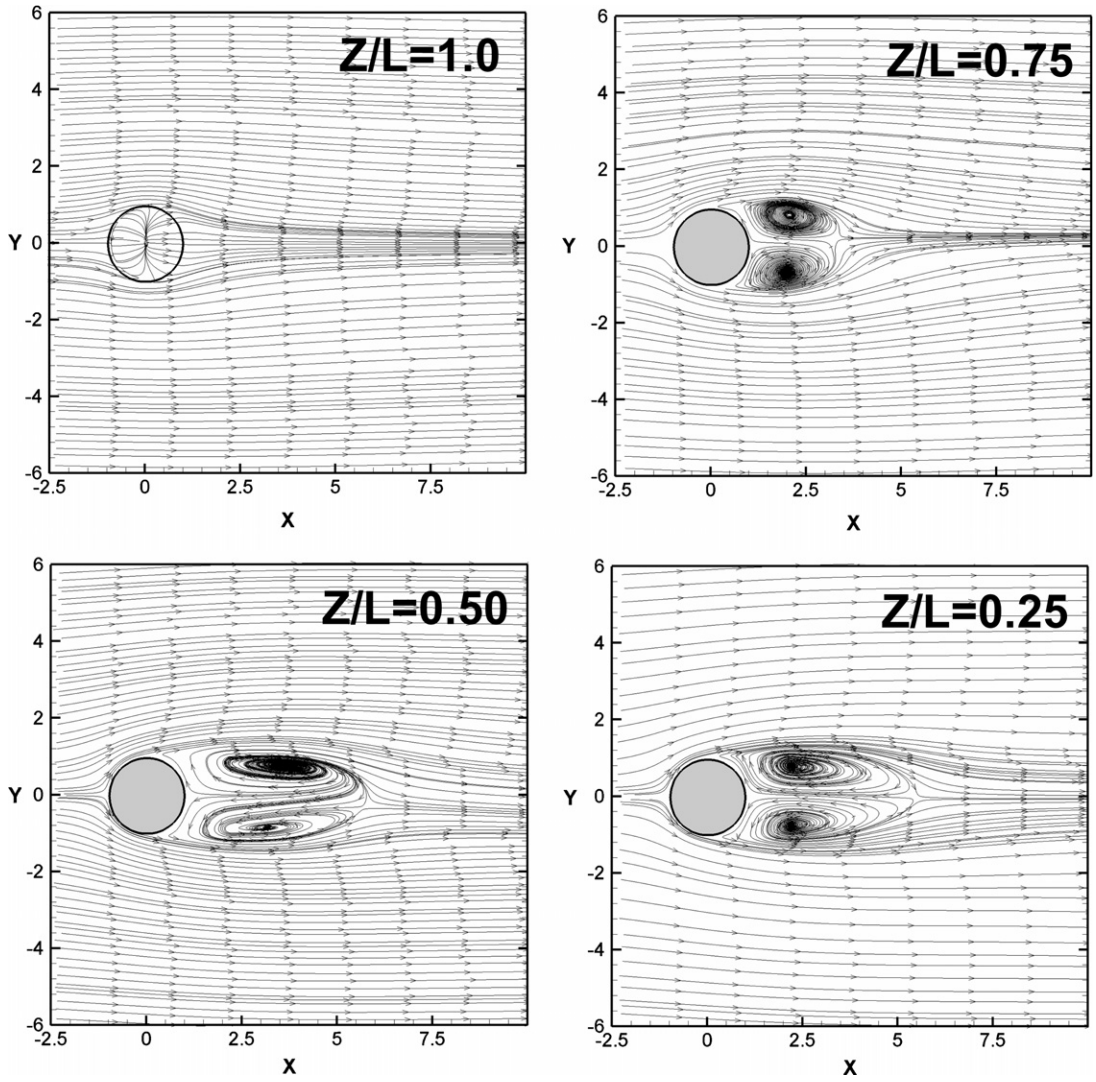

Fig. 6. Streamlines generated from 2D mean velocity vectors in XY planes at various Z/L locations for AR 6 case (FNCM2).

shown as dashed horizontal line shown in Fig. 9c). What is interesting is the heart like shape of the double vortices which, when originated from the tip of the cylinder, are spherical in shape (see Fig. 9a). As they move downstream they are deformed by the strong downwash and the vortex shedding from the sides of the cylinder causing the vortices to converge along the symmetry ($Y = 0$) line thus resulting in perfect heart like shapes (see Fig. 9c). Indeed these structures are a direct consequence of the time averaging of the streamlines and would not have been so clear and well formed in an instantaneous field.

For a much smaller cylinder (AR = 2.5) Frohlich and Rodi (2004) observed an arched vortex structure in the cylinder's wake, which is consistent with the well separated vortex pair in Fig. 9. Investigating the mean vector plots over the tip reveals two counter rotating, oppositely directed, perfectly symmetrical vortices. It is believed that the roll up of the shear flow separation from the free end leads to this counter rotating pair of vortices which later develop into an inverted U structure (as seen in Fig. 9a) causing a

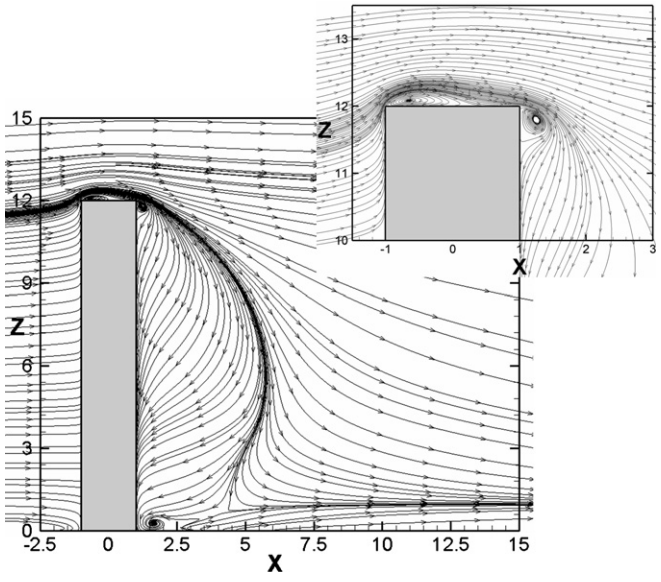

Fig. 7. Streamlines generated from 2D mean velocity vectors in XZ (symmetry) plane for AR 6 case (FNCM2).

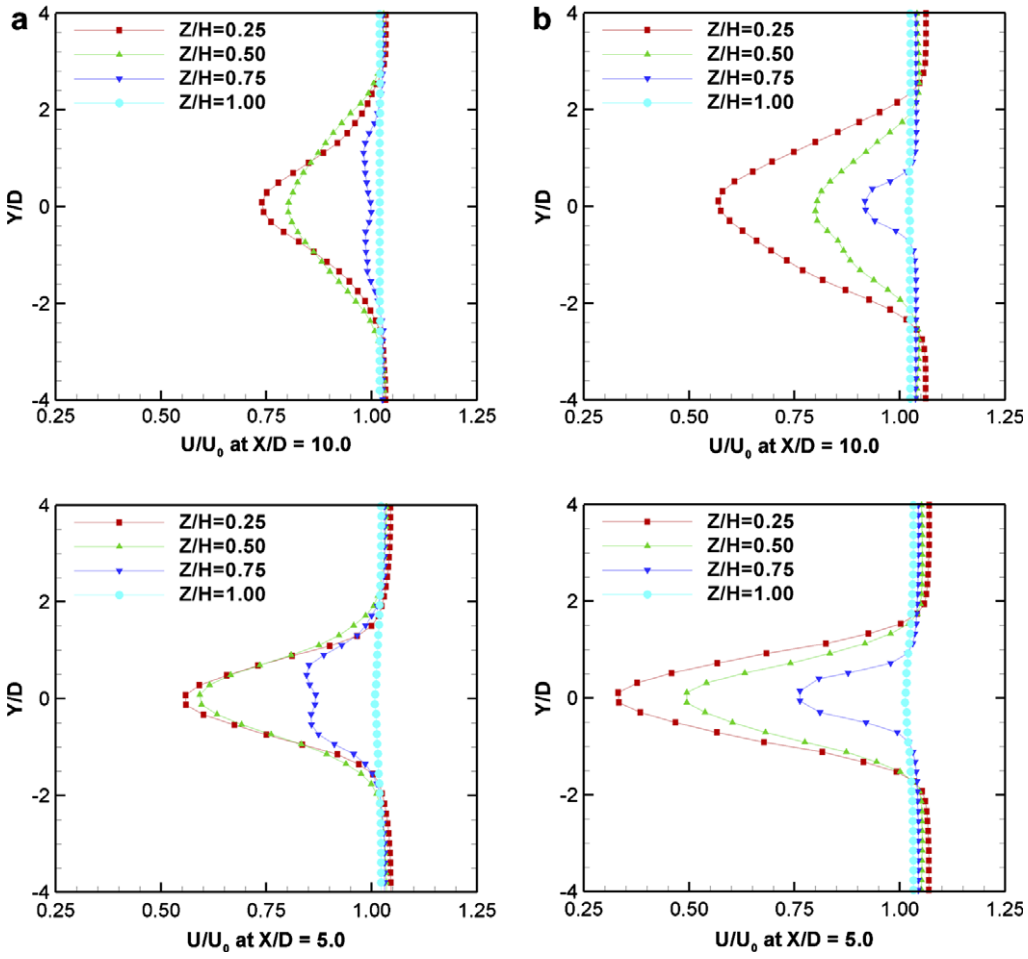

Fig. 8. Mean velocity comparison in the wake of the cylinders at various X/D locations: (a) AR 10 case. (b) AR 6 case.

strong downwash and thus suppressing the vortex shedding from the sides of the cylinder.

Fig. 9 also signifies the fact that for the larger AR case (AR 10) the effect of the tip vortices is not felt near the base of the cylinder and hence no trace of the tip vortices can be observed on the flat plate. For the smaller AR case (AR 6) the effect is shown to travel up to the base of the cylinder (see Fig. 7) somewhat similar to what Frohlich and Rodi (2004) observed. Indeed, the smaller AR of 6 of the present simulations and the AR of 4 of Frohlich and Rodi (2004) are quite comparable both in terms of geometric properties and flow behaviour. The tip effects in both these cases are seen to be overwhelmingly dominant.

Fig. 10a shows the streamlines in XZ symmetry ($Y/D = 0$) plane for the AR 10 case. Here one sees that the recirculation region near the tip of the cylinder is somewhat smaller than the AR 6 case. The instantaneous velocity magnitude plot for the AR 10 case in the XZ plane at $Y/L = 0$ shown in Fig. 10b reveals the vortex columns behind the cylinder which are distorted over 2/3 of the height and even suppressed by the downwash near the tip.

Fig. 11 shows a comparison of velocity magnitudes at $Z/L = 0.3$ (top plots) and $Z/L = 0.8$ (bottom plots) in XY plane. For the smaller aspect ratio case (AR 6, see Fig. 11a) at both $Z/L = 0.3$ and $Z/L = 0.8$ locations, we see a peculiar flow behaviour where the wake splits into two tongues. It is speculated that the strong downwash is directly responsible for this bifurcation of the wake. The phenomenon of classical vortex streets (shedding of one vortex after the other from opposite sides of the cylinder) is being interrupted by the downwash. This causes the flow behaviour on both sides of the cylinder to be independent of each other (unlike a 2D or infinite 3D cylinder). However, for the higher aspect ratio case (AR 10, see Fig. 11b) a different flow phenomenon is observed. Here one sees that near the base (at $Z/L = 0.3$) the cylinder wake behaves as a 2D cylinder with regular vortex shedding from the upper and lower surfaces. Near the tip (at $Z/L = 0.8$) the behaviour is similar to the smaller aspect ratio case. Hence, we conclude that a finite cylinder with aspect ratio 10 shows both finite tip effects and base effects (2D cylinder behaviour) whereas the aspect ratio 6 cylinder does not show any infinite cylinder behaviour, which extends the findings of Frohlich and Rodi (2004) from AR 2.5 to AR 6.

An instantaneous realization of the second invariant of the velocity gradients for the AR 10 case (FNCM1) is shown in Fig. 12. For computations, Q is defined as $Q = -0.5[S_{ij}S_{ij} - \Omega_{ij}\Omega_{ij}]$; Hunt et al. (1988). Herein it is

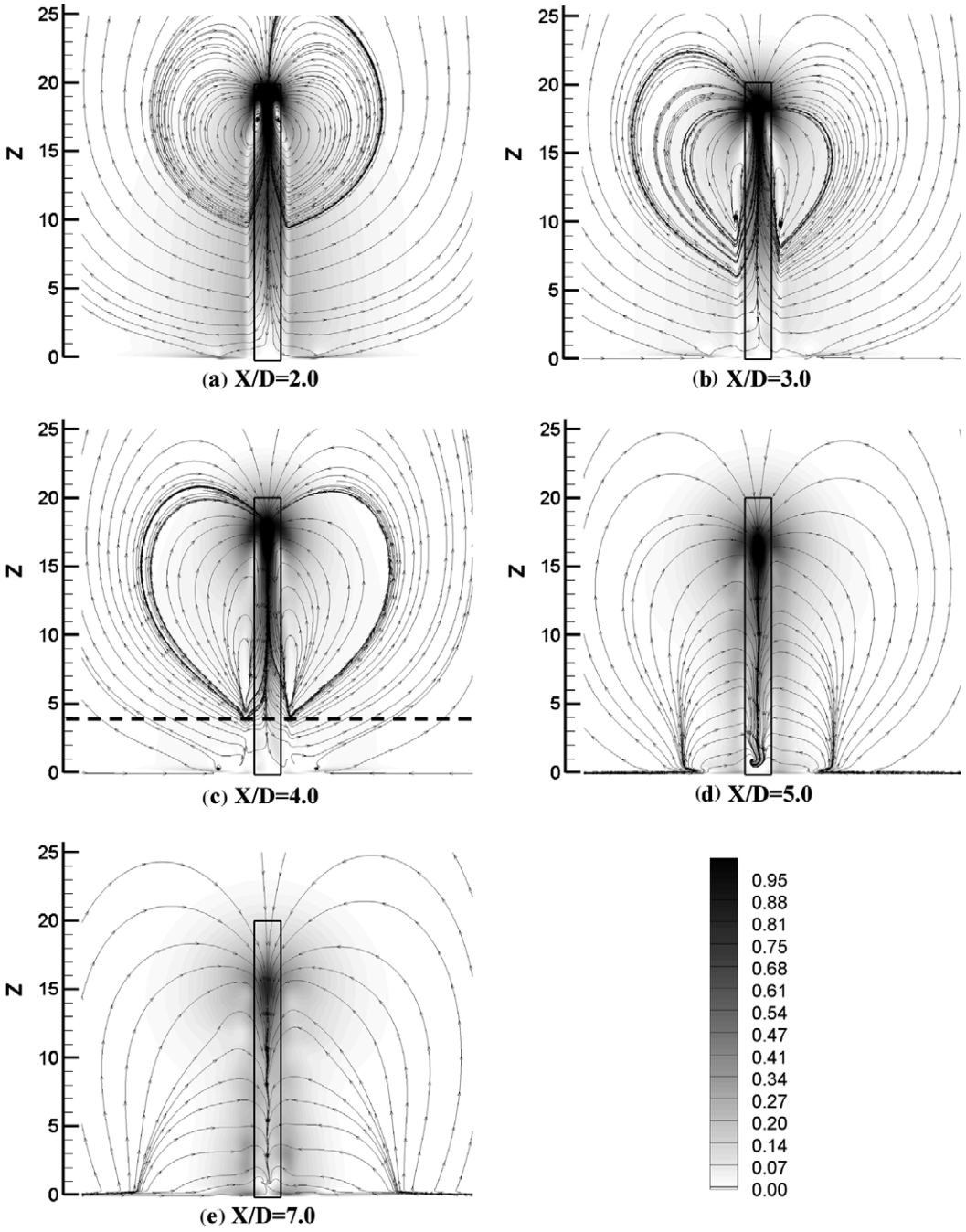

Fig. 9. Averaged pseudo-streamlines behind cylinder at various locations for AR 10 case (FNCM1) along with contours of secondary flow.

normalized as ($Q = \alpha(U_0/L_C)^2$) where α is a non-dimensional constant set by the user in order to obtain desired flow structures and L_C is the characteristic length scale (in current cases the cylinder diameter). For the current plot the constant α is chosen to return a value of $Q = 1$. The figure has been rendered by contours of vorticity in Z direction (ω_z) to show opposite direction of the coherent structures. Near the base of the cylinder we see the trace of the horseshoe vortex as well which is very well defined but was difficult to observe in other instantaneous snapshots. Near the tip of the cylinder the downwash causes a sharp decrease in the turbulence intensity and hence smaller and less structures are seen. Interestingly the Iso-Q structures reveal the difference in the flow behaviour for the two cases. For the AR 6 (see Fig 12a) one notices some of the larger structures travelling up to the base plate, with a majority of them being concentrated near the base plate. However, for AR 10 case these structures are seen to be shorter in size and more concentrated near the downstream of the wake. Clearly the effect of the downwash (which is much stronger for the smaller aspect ratio case) is dictating this flow behaviour. This is further supported by observing

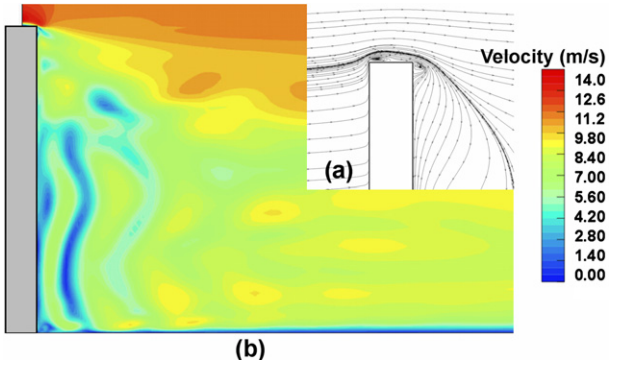

Fig. 10. XZ sectional views at $Y/D = 0$ for AR 10 case (FNCM1): (a) Averaged pseudo-streamlines. (b) Instantaneous velocity magnitude.

Fig. 12a and b which show that for the same Iso-Q value the downstream of the cylinder wakes shows a large difference in the mere volume of these coherent structures.

5.3. Lift, drag and turbulence intensity

The full three-dimensionality of the flow and irregular and intermittent vortex shedding cause highly fluctuating lift (C_L) and drag (C_D) forces on the cylinder surface (see Fig. 13a), where the coefficients are computed using the projected area (A) of the cylinder and the free stream inlet velocity (U_0). The lift and drag coefficients show a varying amplitude and intensity and hence require substantially long averaging times, similar to the findings of Frohlich and Rodi (2004), but in their case the AR was 2.5 and hence the lift displayed a non-zero local average, forcing them to time average over an even longer period thus making the computations more expensive.

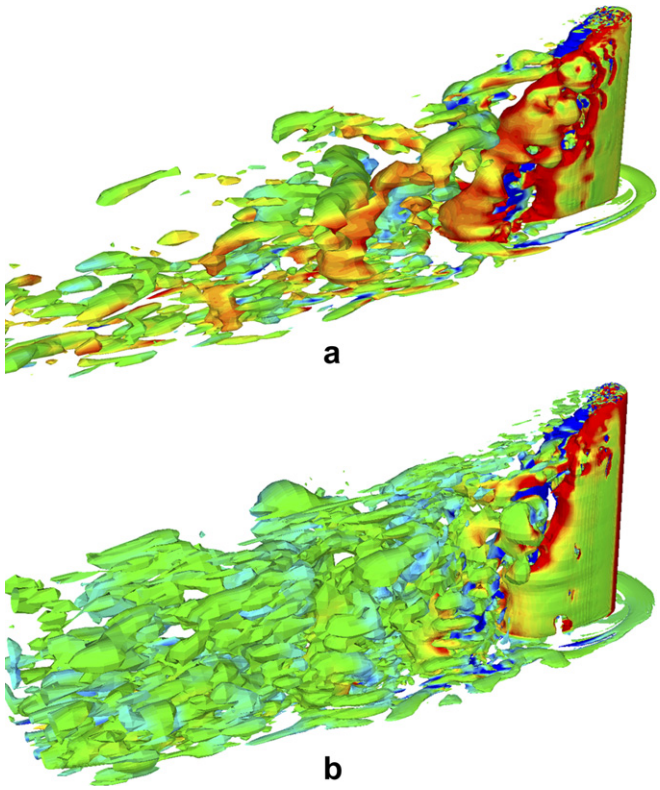

Fig. 12. Second invariant of the velocity gradients ($Q = 1$) rendered by contours of vorticity [$\omega_Z = (\mathrm{d}u/\mathrm{d}y) - (\mathrm{d}v/\mathrm{d}x)$.] (a) AR 6 case (FNCM2). (b) AR 10 case (FNCM1).

The streamwise (F_X) and normal (F_Y) forces are the sum of the integrated wall pressure and the cylinder surface friction forces, where the contribution of the latter is found to

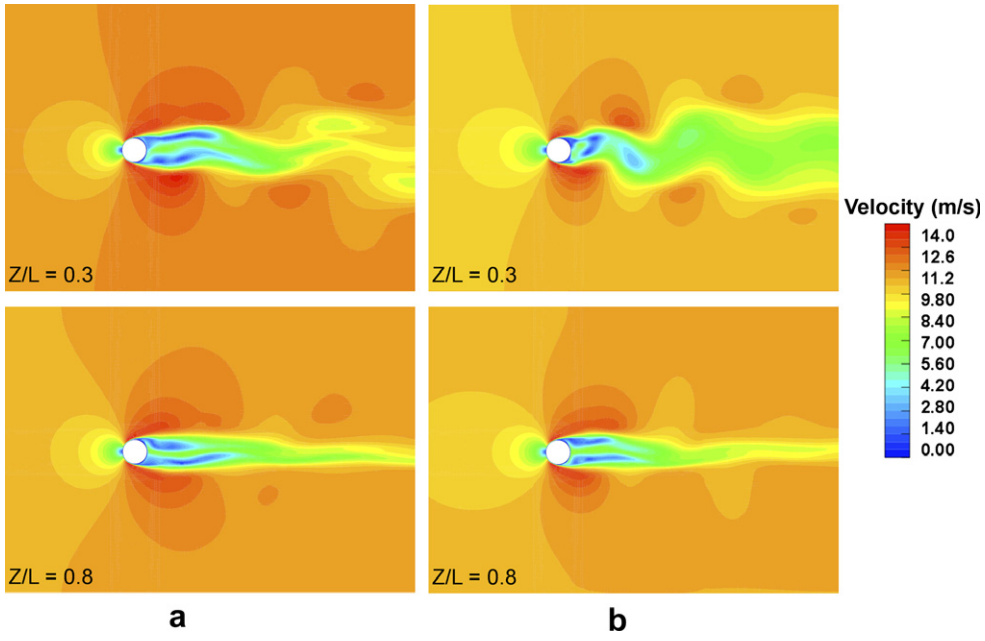

Fig. 11. Instantaneous velocity magnitude comparison between $Z/L = 0.3$ (top plots) and $Z/L = 0.8$ (bottom plots) in XY plane: (a) AR 6 case (FNCM2). (b) AR 10 case (FNCM1).

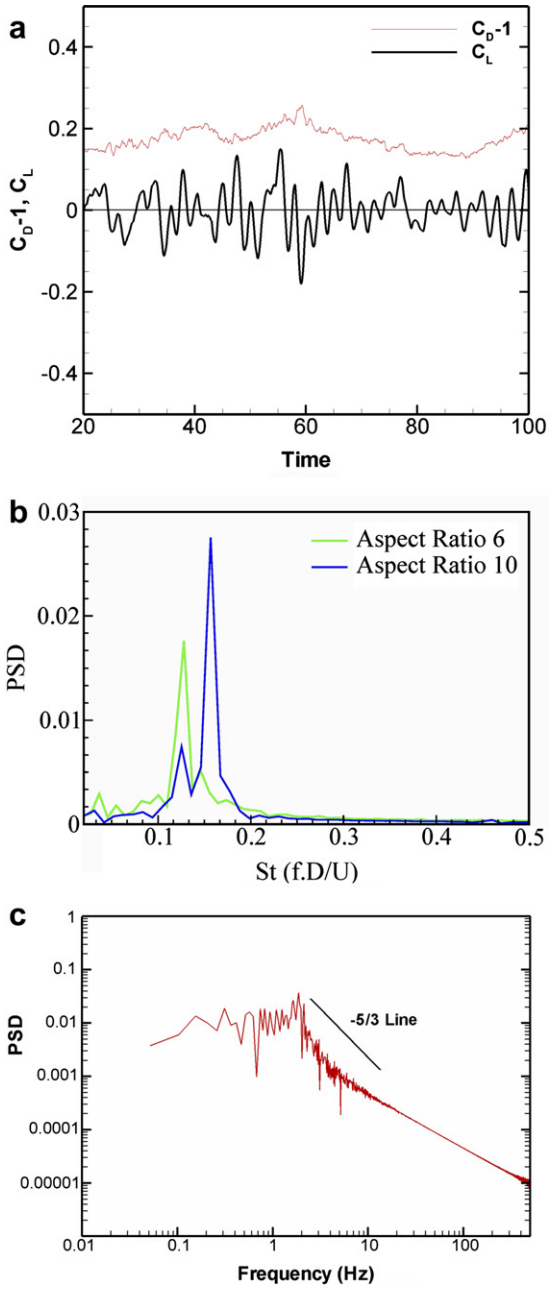

Fig. 13. (a) Lift and drag curves for AR 10 case (FNCM1). (b) PSD of lift coefficient for both cases (AR 10 FNCM1 and AR 6 FNCM2). (c) PSD of lift coefficient for AR 10 case shown on a log–log scale.

Table 2
Strouhal number comparison

Park and Lee (2000, 2002, 2004)		LES
AR 6	0.135	0.132
AR 10	0.159	0.167

be less than 5% of the total force and hence this friction component is commonly ignored while calculating the streamwise or drag coefficient; Kawamura et al. (1984).

Findings of Park and Lee (2000, 2002) report that the vortex shedding frequency decreases as the aspect ratio of the cylinder decreases where a 2D cylinder has a Strouhal number of 0.198. A similar trend is seen in the numerical computations, where the Power Spectrum Density analysis (PSD) of the lift coefficient is used to capture the Strouhal numbers for both cases (see Fig. 13b). A comparison between experimental (Park and Lee, 2000, 2002, 2004) and numerical Strouhal numbers given in Table 2 shows a good agreement. To check the degree of accuracy of the numerical results the PSD of AR 10 case was then plotted against the frequency (Hz) on a log–log scale which is shown in Fig. 13c. The slope of the spectrum curve is shown to be in good agreement with a line of $-5/3$ slope.

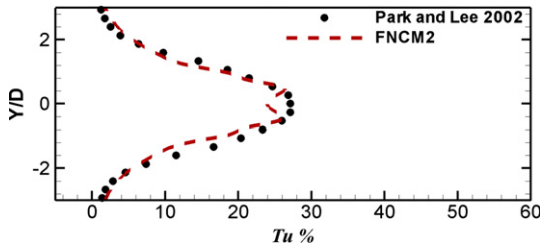

Fig. 14. Streamwise turbulence intensity (Tu%) at $Z/L = 0.5$ and $X/D = 5$ for AR 6 case.

A comparison between numerically and experimentally obtained mean streamwise turbulence intensity percentage (Tu%) at $Z/L = 0.5$ location in the wake of the cylinder ($X/D = 5$) for the lower aspect ratio case is shown in Fig. 14. The experimental data taken from Park and Lee (2002) shows a peak value of 28% whereas the LES simulation shows a double peak of 26%. The DES by Strelets (2005) also shows a double peak but with a slightly lower

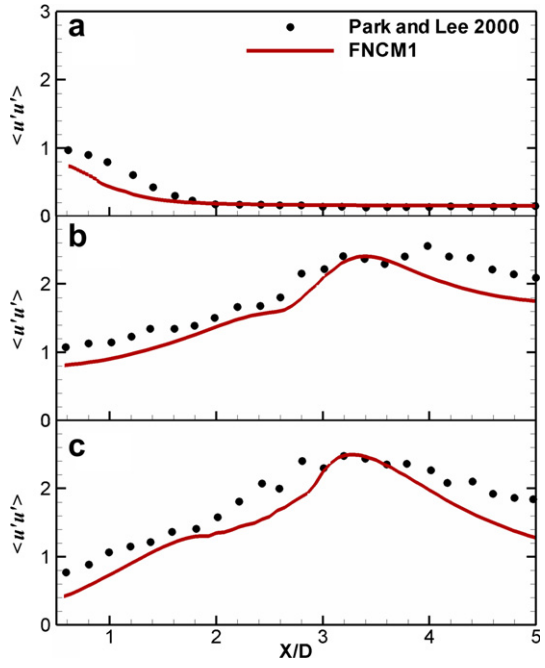

Fig. 15. $\langle u'u' \rangle$ at various Z/L locations for AR 10 case along $Y/D = 0$ line. (a) $Z/L = 0.950$. (b) $Z/L = 0.625$. (c) $Z/L = 0.125$.

maxima. Interestingly all DESIDER project numerical simulations (DES by Strelets (2005) and very fine LES by Krajnovic (2006), not shown here) predict a double peak for turbulence intensity at this location. This is due to the fact that a slightly longer recirculation region is predicted by all numerical simulations in the wake of the cylinder (as seen in Fig. 6).

A comparison of streamwise turbulence intensity $\langle u'u' \rangle$ at various Z/L locations for the higher aspect ratio case is shown in Fig. 15. One notices that the streamwise turbulence intensities are slightly under-predicted even though the pressure and velocity comparisons were well captured. However, the general trend and the length of the vortex formation region are still predicted accurately. The slight under prediction in numerical results may be attributed to grid coarsening in the wake. The grid has a sufficient resolution near the wall in the wake of the cylinder ($Y^+ = 1$) but the grid distribution downstream becomes somewhat coarse. Secondly, the Smagorinsky model is not suitable for prediction of laminar to turbulent transition (Fig. 12 gives some indication that the separating shear layer remains laminar over some distance).

We observe that the streamwise turbulence intensities increase while moving towards the fixed end of the cylinder, where the maximum values are behind the lower half of the cylinder (see Fig. 15). This confirms the initial observation that the effect of the strong down wash is to reduce the turbulence intensity and vortex formation region in the upper half of the cylinder; $\langle u'u' \rangle$ is reduced to almost one-third in magnitude (see Fig. 15). This is confirmed in the experiments and is similar to the observations of Frohlich and Rodi (2004).

6. Conclusions

The flow over a cantilever cylinder mounted vertically on a flat plate was numerically simulated by LES for aspect ratios of 6 and 10. Numerical results were compared to experimental data of Park and Lee (2000, 2002, 2004). The use of multiple levels of local refinements with the *STAR-CD* code enabled the simulation of such a complex geometry using only 2.6 million cells whereas for a regular grid LES requirement would be at least 10 times higher. Despite the high aspect ratio, the flow over both the cylinders is found to be strongly inhomogeneous along the height of the cylinders, i.e. highly three-dimensional and significantly more turbulent in the lower half of the wake. The roll up of the shear layer separation from the free end causes two counter rotating vortices near the free end of the cylinder leading to a strong downwash extending downstream nearly to the base. This downwash changes the flow evolution by interacting with the regular vortices being shed from the sides of the cylinder. This interaction causes changes in the pressure distribution in the wake of the cylinder and damping of the vortex shedding.

For the smaller aspect ratio case the effect of the downwash is stronger, and the tip effect is felt all along the cylinder height. The wake is split into two entirely independent elongated recirculations separated by a large backflow region along the symmetry axis, significantly different from the infinite cylinder case. On the other hand for the higher aspect ratio case the effect of the downwash is limited to the top half of the cylinder and hence the interaction is weaker causing pressure recovery in the wake of the cylinder with regular vortex shedding. The flow pattern at the very tip of the cylinders surprisingly changes between AR 6 and 10, with the latter showing stronger pressure recovery due to backflow in the vertical plane. The Strouhal number also shows significant variations. Even for the higher AR case, the C_P profile at mid-height is significantly different from that of an infinite cylinder.

Acknowledgements

Authors are grateful to C.W. Park and S.J. Lee for provision of experimental data and clarification of its use, as well as discussions with M. Strelets and S. Krajnovic (partners in DESider). This work has been partly supported by DESider project funded by European Union under Contract No. AST3-CT-2003-502842. (http://cfd.me.umist.ac.uk/desider)

References

Afgan, I., Moulinec, C., Laurence, D., 2006. Large eddy simulation of flow over a vertically mounted finite cylinder on a flat plate. In: 13th International Conference on Fluid Flow Technologies, CMFF '06, Budapest, Hungary, pp. 193–200.

Benhamadouche, S., Laurence, D., 2003. LES, coarse LES, and transient RANS comparisons on the flow across tube bundle. Int. J. Heat Fluid Flow 4, 470–479.

Benhamadouche, S., Laurence, D., Jarrin, N., Afgan, I., Moulinec, C., 2005. Large Eddy Simulation of Flow Across In-line Tube Bundles. NURETH-11, Avignon, France.

Bouris, D., Bergeles, G., 1999. Two dimensional time dependent simulation of the subcritical flow in a staggered tube bundle using a subgrid scale model. Int. J. Heat Fluid Flow 20 (2), 105–114.

Farivar, D., 1981. Turbulent uniform flow around cylinders of finite length. J. AIAA J. 19, 275–281.

Ferziger, J.H., Peric, M., 2002. Computational Methods for Fluid Dynamics, third ed. Springer.

Frohlich, J., Rodi, W., Kessler, P., Parpais, S., Bertoglio, J., Laurence, D., 1998. Large eddy simulation of flow over circular cylinders on structured and unstructured grids. In: Hirschel, E. (Ed.), Numerical Flow Simulation I, Notes on Numerical Fluid Mechanics, vol. 66. Vieweg, pp. 319–338.

Frohlich, J., Rodi, W., 2004. LES of flow around a circular cylinder of finite height. Int. J. Heat Fluid Flow 25, 537–548.

Grotzbach, G., Worner, M., 1999. Direct numerical and large eddy simulations in nuclear applications. Int. J. Heat Fluid Flow 20, 222–240.

Hunt, J.C.R., Wray, A.A., Moin, P., 1988. Eddies, stream and convergence zones in turbulent flows. Report CTR-S88. Center for Turbulent Research.

Kawamura, T., Hiwada, M., Hibino, T., Mabuchi, I., Kamuda, M., 1984. Flow around a finite circular cylinder on a flat plate. Bull. JSME 27 (232), 2142–2151.

Krajnovic, S. 2006. Private Communications (results and publications available on <http://cfd.me.umist.ac.uk/desider>).

Kravchenko, A.G., Moin, P., 1997. On the effect of numerical errors in large eddy simulation of turbulent flows. J. Comput. Phys. 131, 310–322.

Laurence, D., 2006. Large eddy simulation with unstructured finite volumes. In: Lamballais, E., Friedrich, R., Geurts, B.J., Métais, O. (Eds.), Direct and Large-Eddy Simulation VI, ERCOFTAC Series, vol. 10. Springer, pp. 27–38.

Moin, P., Kim, J., 1982. Numerical investigation of turbulent channel flow. J. Fluid Mech. 118, 341–377.

Moulinec, C., Benhamadouche, S., Laurence, D., Peric, M., 2005. LES in a U-bend pipe meshed by polyhedral cells. ERCOFTAC ETMM-6 Conference. Elsevier, Sardinia.

Okajima, A., Kosugi, T., Nakamura, A., 2002. Flow-induced in-line oscillation of a circular cylinder in a water tunnel. J. Pressure Vessel Technol., ASME 124, 89–96.

Park, C.W., Lee, S.J., 2000. Free end effect on the wake flow structure behind a finite circular cylinder. J. Wind Eng. Ind. Aerodyn. 88, 231–246.

Park, C.W., Lee, S.J., 2002. Flow structure around a finite circular cylinder embedded in various atmospheric boundary layers. Fluid Dynam. Res. 30, 197–215.

Park, C.W., Lee, S.J., 2004. Effects of free-end corner shape on flow structure around a finite cylinder. J. Fluids Struct. 19, 141–158.

Pope, S.B., 2000. Turbulent Flows, first ed. Cambridge University Press.

Rhie, C., Chow, W., 1982. A numerical study of the flow past an isolated airfoil with trailing edge separation. J. AIAA 21, 1525–1532.

Strelets, M. 2005. Private Communications (results and publications available on <http://cfd.me.umist.ac.uk/desider>).

Van Doormal, J.P., Raithby, G.D., 1984. Enhancements of the SIMPLE method for predicting incompressible fluid flows. Numer. Heat Transfer 7, 147–163.

Zdravkovich, M.M., Brand, V.P., Mathew, G., Weston, A., 1989. Flow past short circular cylinders with two ends free. J. Fluid Mech. 203, 557–575.

Zdravkovich, M., 1997. Flow Around Circular Cylinders. Oxford University Press.